

# Understanding Future Increases in Precipitation Extremes in Global Land Monsoon Regions

MEIYU CHANG,<sup>a</sup> BO LIU,<sup>a</sup> BIN WANG,<sup>b,c</sup> CRISTIAN MARTINEZ-VILLALOBOS,<sup>d</sup> GUOYU REN,<sup>a,e</sup> AND TIANJUN ZHOU<sup>f</sup>

<sup>a</sup> *Department of Atmospheric Science, School of Environmental Studies, China University of Geosciences, Wuhan, China*

<sup>b</sup> *Department of Atmospheric Sciences, University of Hawai'i at Mānoa, Honolulu, Hawaii*

<sup>c</sup> *Earth System Modeling Center, Nanjing University of Information Science and Technology, Nanjing, China*

<sup>d</sup> *Faculty of Engineering and Science, Universidad Adolfo Ibañez, Santiago, Chile*

<sup>e</sup> *Laboratory for Climate Studies, National Climate Center, China Meteorological Administration, Beijing, China*

<sup>f</sup> *LASG, Institute of Atmospheric Physics, Chinese Academy of Science, Beijing, China*

(Manuscript received 27 May 2021, in final form 1 December 2021)

**ABSTRACT:** This study investigates future changes in daily precipitation extremes and the involved physics over the global land monsoon (GM) region using climate models from phase 6 of the Coupled Model Intercomparison Project (CMIP6). The daily precipitation extreme is identified by the cutoff scale, measuring the extreme tail of the precipitation distribution. Compared to the historical period, multimodel results reveal a continuous increase in precipitation extremes under four scenarios, with a progressively higher fraction of precipitation exceeding the historical cutoff scale when moving into the future. The rise of the cutoff scale by the end of the century is reduced by 57.8% in the moderate emission scenario relative to the highest scenario, underscoring the social benefit in reducing emissions. The cutoff scale sensitivity, defined by the increasing rates of the cutoff scale over the GM region to the global mean surface temperature increase, is nearly independent of the projected periods and emission scenarios, roughly  $8.0\% \text{ K}^{-1}$  by averaging all periods and scenarios. To understand the cause of the changes, we applied a physical scaling diagnostic to decompose them into thermodynamic and dynamic contributions. We find that thermodynamics and dynamics have comparable contributions to the intensified precipitation extremes in the GM region. Changes in thermodynamic scaling contribute to a spatially uniform increase pattern, while changes in dynamic scaling dominate the regional differences in the increased precipitation extremes. Furthermore, the large intermodel spread of the projection is primarily attributed to variations of dynamic scaling among models.

**KEYWORDS:** Precipitation; Extreme events; Monsoons; Climate prediction; Thermodynamics; Dynamics

## 1. Introduction

The intensity of extreme precipitation is projected to increase with a much higher rate than the mean precipitation as the climate warms, close to the increasing rate ( $7.5\% \text{ K}^{-1}$ ) of atmospheric water vapor content (Allen and Ingram 2002; Trenberth et al. 2003; Pall et al. 2007; Pendergrass et al. 2015; Giorgi et al. 2019). During past decades, great efforts have been devoted to investigating changes in the mean and extreme precipitation over monsoon regions as monsoon-related rainfall supports nearly 62% of the global population (Vera et al. 2006; Kitoh et al. 2013; Zhang et al. 2018; Ni and Hsu 2018; Deng et al. 2018; Seth et al. 2019; Zhang and Zhou 2019; Moon and Ha 2020; Chen et al. 2020; Wang et al. 2020). As indicated by Fig. 1, the global land monsoon (GM) region includes seven major land monsoon regions: the northern Africa, southern Africa, South Asia, East Asia, Australia, North America, and South America monsoon regions. Over the GM region, the mean response rates of Rx1day (the annual maximum 1-day precipitation) and Rx5day (the

annual maximum 5-day precipitation) for the period 1901–2010 are estimated to be  $7.5\%$  and  $4.8\% \text{ K}^{-1}$ , respectively (Zhang and Zhou 2019). This excessive increase in extreme precipitation can aggravate the flood risk over the monsoon regions and bring severe societal and economic losses (Kirsch et al. 2012; IPCC 2014; Mishra and Shah 2018). For example, on 21 July 2012, the extreme precipitation that occurred in Beijing led to an enormous economic loss of nearly \$2 billion (Zhang et al. 2013). Thus, providing a reliable assessment for the changes in extreme precipitation over the GM region and understanding the involved physical mechanisms are essential to improving future prospects of food risk and disaster mitigation.

Conventional thresholds, such as the 95th or 99th percentile of precipitation (R95p, R99p), Rx1day, and Rx5day, are often used as the criteria to investigate the future changes of extreme precipitation (Kitoh et al. 2013; Freychet et al. 2015; Wu et al. 2015; Zhang et al. 2018; Chevuturi et al. 2018; Lee et al. 2018; Lui et al. 2019; Ha et al. 2020). These indices are used for practical reasons (e.g., risk assessment) but are not physically motivated. Moreover, quantitative conclusions are generally index-dependent. For example, multimodel results show that during the period 2006–2100, the linear trends of global mean R95p and Rx5day over land under global warming are  $21.1\%$  and  $4.9\% \text{ K}^{-1}$ , respectively (Wang et al. 2017). In central India, robust enhancements of Rx5day ( $11.3\% \text{ K}^{-1}$ ) and R95p ( $8.47\% \text{ K}^{-1}$ ) can be found during the 2075–99

Supplemental information related to this paper is available at the Journals Online website: <https://doi.org/10.1175/JCLI-D-21-0409.s1>.

Corresponding author: Bo Liu, [boliu@cug.edu.cn](mailto:boliu@cug.edu.cn)

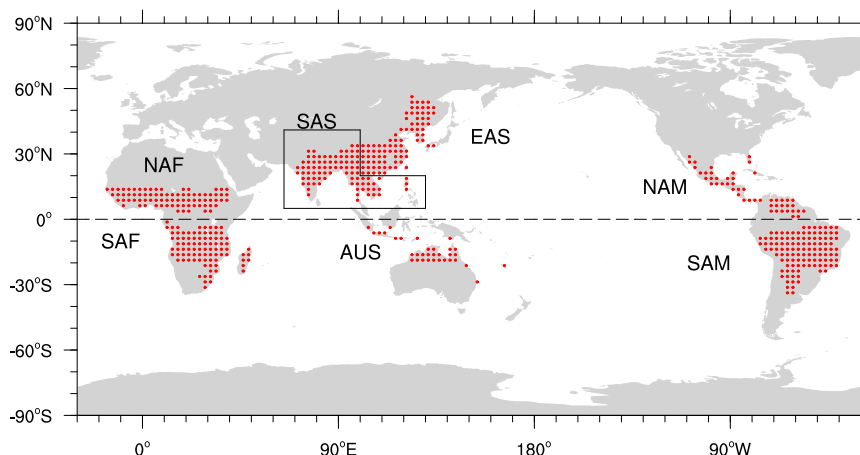


FIG. 1. The global land monsoon region (red dots) defined according to rainfall characteristics based on monthly GPCP precipitation for the period 1979–2014. The equator (dashed line) separates the Northern Hemisphere land monsoon region (NAF, SAS, EAS, and NAM) from the Southern Hemisphere land monsoon region (SAF, AUS, and SAM), and SAS and EAS are separated by 20°N and 100°E.

period, relative to the period 1979–2003 (Lui et al. 2019). Over China, R99p and R95p are reported to increase about 21.6% and 11.9%  $K^{-1}$  in the period 2006–99 relative to the period 1961–2005 (Wu et al. 2015). Moreover, it should be noted that these indices (e.g., uniform R95p, R99p) may have different implications in different regions (Pendergrass 2018). For instance, in San Diego, California, where the events with precipitation exceeding the 95th percentile account for almost 90% of total annual precipitation (Pendergrass 2018), we can hardly use R95p as the extreme index there. In other words, changes of a specific percentile may not accurately reflect changes in the extreme tail of the probability distribution of precipitation (Contractor et al. 2018; Alexander et al. 2019).

Motivated by these limitations, the cutoff scale is proposed to be used as the indicator of precipitation extremes (Deluca and Corral 2010, 2014; Peters et al. 2001, 2010; Stechmann and Neelin 2011, 2014; Neelin et al. 2017; Martinez-Villalobos and Neelin 2018). With the increase of precipitation size, the probability density function (PDF) of daily precipitation gradually decays and sharply falls after a characteristic cutoff scale (Martinez-Villalobos and Neelin 2019, 2021; Chang et al. 2020). Hence, the extreme tail in precipitation PDF can be directly indicated by the cutoff scale. Physically, the existence of the cutoff scale is due to the balance between precipitation loss and variation of moisture convergence (Neelin et al. 2017; Martinez-Villalobos and Neelin 2019). The cutoff scale may correspond to different precipitation percentiles (Chang et al. 2020). As moisture convergence variance increases with global warming, the upshift in the extreme tail of the probability distribution can be well represented by an extension of the cutoff scale (Neelin et al. 2017; Martinez-Villalobos and Neelin 2018; Chang et al. 2020), which provides insight into future changes in precipitation extremes. For this reason, it is of interest to use the cutoff scale to explore the future

changes in precipitation extremes and the associated uncertainties in the GM and individual monsoon regions.

To understand the underlying mechanisms explaining changes in the cutoff scale, we use a physical scaling diagnostic to decompose precipitation extremes into thermodynamic and dynamic components (O’Gorman and Schneider 2009a,b; Sugiyama et al. 2010). This method has been proved to be effective in quantifying the contributions of thermodynamics and dynamics in precipitating processes (Pfahl et al. 2017; Ali and Mishra 2018).

The remainder of this study is organized as follows. Descriptions of datasets and methods are provided in section 2. Section 3 presents the projected increases of extreme precipitation and further reveals the contributions of dynamics and thermodynamics in these changes. Finally, concluding remarks are given in section 4.

## 2. Data and methods

### a. Model data

In this study, the CMIP6 archive (Eyring et al. 2016) is used as the primary dataset to investigate future changes in precipitation extremes. We have first evaluated the performance of the 25 available CMIP6 models in simulating monsoon precipitation during the historical period 1995–2014 according to the metrics proposed by previous studies (Wang and Ding 2008; Wang et al. 2020), namely, the annual mean, summer [June–September (JJAS)] mean, winter [December–March (DJFM)] mean, and summer-minus-winter precipitation (see Figs. S1–S4 in the online supplemental material). Finally, we chosen 21 models with better performance (Table S1 in the online supplemental material). To examine changes in cutoff scale, we use daily precipitation and monthly surface temperature from 21 CMIP6 models, including the historical simulations and the projections

under four scenarios, namely the Shared Socioeconomic Pathway 1–2.6 (SSP1–2.6), SSP2–4.5, SSP3–7.0, and SSP5–8.5 (O'Neill et al. 2016; Table S1). The historical period 1995–2014 and three future periods, referred to as the near-term (2021–40), midterm (2041–60), and long-term (2080–99) periods, are used for the analysis.

In applying the precipitation extremes scaling, daily air temperature and vertical velocity at all eight pressure levels (1000, 850, 700, 500, 250, 100, 50, and 10 hPa) and monthly surface pressure from 15 out of 21 CMIP6 models are used. Note that only one realization of each model is used, although we discuss the effect of using more realizations (see below). The resulting fields from each model are interpolated to a grid of  $2.5^\circ \times 2.5^\circ$  to calculate the multimodel ensemble mean.

### b. Definition of the GM region

Following Wang et al. (2011), we have defined the GM domain as the regions where the local summer-minus-winter precipitation intensity exceeds  $2.5 \text{ mm day}^{-1}$  and the ratio of summer total to annual total precipitation is greater than 55%. Here, the summer is from May to September, and the winter is from November to March in the Northern Hemisphere, and vice versa in the Southern Hemisphere. The GM domain (Fig. 1), used in this study, is calculated based on the monthly precipitation data from the Global Precipitation Climatology Project version 2.3 (GPCP v2.3; Adler et al. 2003) for the period 1979–2014. We also calculated the monsoon region based on the multimodel mean monthly precipitation of the 21 CMIP6 models for the period 1995–2014, and there is almost no difference in GM domain between the two datasets (Fig. S5). Moreover, the GM domain can be divided into seven subregions, the northern Africa (NAF), southern Africa (SAF), South Asia (SAS), East Asia (EAS), Australia (AUS), North America (NAM), and South America (SAM) monsoon regions (Fig. 1).

### c. Cutoff scale and daily precipitation PDF

As previous studies have shown, the probability of daily precipitation intensity ( $p_P$ ) tends to follow gamma distributions (Cho et al. 2004; Martinez-Villalobos and Neelin 2019):

$$p_P \propto P^{-\tau_P} \exp(-P/P_L), \quad (1)$$

where  $P$  represents daily precipitation,  $\tau_P$  is the power-law exponent controlling the decline rate of the precipitation PDF in the low and moderate range, and  $P_L$  is the cutoff scale of daily precipitation, where the probability density starts to decline sharply.

The daily precipitation cutoff  $P_L$  is found to be proportional to the moment ratio  $P_M$  (Stechmann and Neelin 2014; Neelin et al. 2017; Martinez-Villalobos and Neelin 2019), which is defined as

$$P_M = \frac{\langle P^2 \rangle}{\langle P \rangle}, \quad (2)$$

with  $\langle P^2 \rangle$  and  $\langle P \rangle$  representing the variance and mean over all wet days ( $P \geq 0.1 \text{ mm}$ ).

To quantify the risk of extreme precipitation, we calculate the risk ratio (e.g., Neelin et al. 2017) between the future period and the historical period, expressed as

$$r_P(\hat{P}) = \frac{\int_{\hat{P}}^{\infty} p''_P dP'}{\int_{\hat{P}}^{\infty} p'_P dP'}. \quad (3)$$

The term  $r_P(\hat{P})$  is the conditional ratio of probability of the daily precipitation larger than  $\hat{P}$ , with  $p''_P$  and  $p'_P$  representing the probability density of the future period and the historical period (over wet days), respectively. If  $r_P(\hat{P}) > 1.0$  [ $r_P(\hat{P}) < 1.0$ ], a higher (lower) fraction of precipitation larger than  $\hat{P}$  can be found in the future period.

### d. Precipitation extremes scaling

A physical scaling diagnostic is applied to decompose them into thermodynamic and dynamic contributions and to understand the reasons for the changes in precipitation extremes. As described by previous studies (O'Gorman and Schneider 2009a; Pfahl et al. 2017), extreme precipitation  $P_e$ , greater than the cutoff scale in this study, at each grid point can be estimated by a vertical integration of the product of the corresponding vertical velocity  $\omega_e$  and vertical derivative of saturation specific humidity  $q_s$  when the saturation equivalent potential temperature  $\theta^*$  is constant:

$$P_e \sim - \left\{ \omega_e \frac{dq_s}{dp} \right\}_{\theta^*}, \quad (4)$$

where  $\{\cdot\}$  represents the mass-weighted vertical integration over tropospheric levels with ascending motion ( $\omega_e < 0$ ). Here the tropopause is defined as the highest level with the lapse rate of  $2 \text{ K km}^{-1}$  and below 50 hPa. The right-hand term of (4) is an estimation of the column-integrated net condensation rate. The thermodynamic scaling can be estimated by keeping the vertical velocity  $\omega_e$  as constant (i.e., the mean value of all days when extreme precipitation occurs in the historical period of 1995–2014), while dynamic contribution can be achieved by subtracting the changes in thermodynamic scaling from the changes in the full scaling.

## 3. Results

### a. Climatology of daily precipitation cutoff scale

Figure 2 gives the spatial distribution of multimodel ensemble mean values of  $P_M$  for the period 1995–2014. High values are found in India, East Asia, Australia, the West African monsoon region, southeastern Africa, and subtropical South America (Fig. 2a), and  $P_M$  has moderate values in the equatorial regions where mean rainfall is high. Even though the modeled  $P_M$  absolute values may deviate from observations (Martinez-Villalobos and Neelin 2021), the spatial distribution of  $P_M$  resembles that of the Rx1day from gauge-based gridded data (Fig. S6). For seven monsoon subregions, when

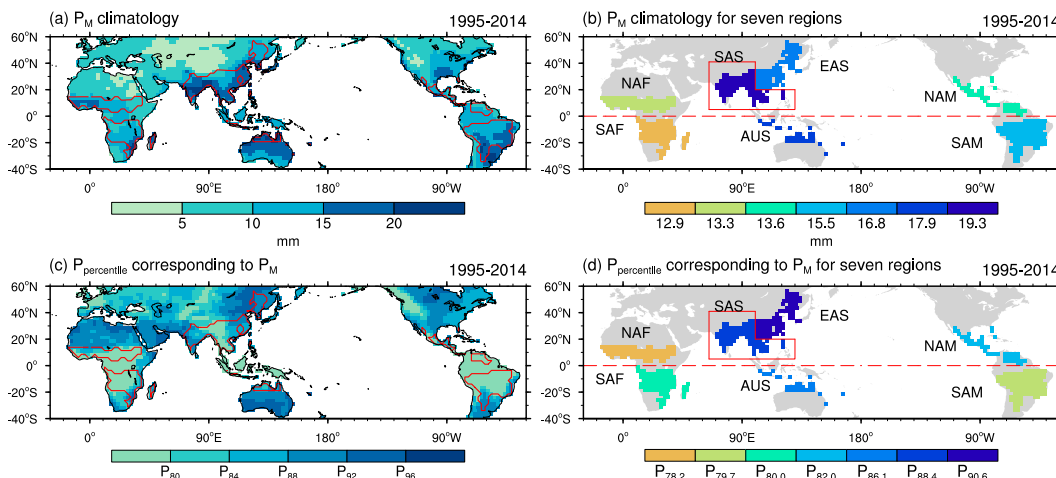


FIG. 2. Multimodel mean of (a)  $P_M$  climatology at each grid point and (b)  $P_M$  climatology for the seven monsoon regions during the historical period 1995–2014. Multimodel mean of the nearest precipitation percentile to the cutoff scale  $P_M$  (with a 0.1-percentile interval) (c) for each grid point and (d) seven monsoon regions during the historical period 1995–2014. The red lines in (a) and (c) denote the boundaries of global land monsoon region.

taking each region as a whole, larger values are located in the SAS, AUS, and EAS monsoon regions, while smaller values are found in the SAM, NAF, NAM, and SAF monsoon regions (Fig. 2b). Moreover, the spatial correlations (the median value of 21 models) between  $P_M$  and the 99th and 99.9th percentiles of daily precipitation ( $P_{99}$  and  $P_{99.9}$ ) over the GM region are all greater than 0.85, significant at 95% confidence interval, for all periods and scenarios (Fig. S7). This indicates that  $P_M$  accurately represents the high percentiles of precipitation (i.e., extreme precipitation). As mentioned above, the values of the cutoff scale, representing the interplay between column moisture convergence and moisture loss (by precipitation), vary with local climate conditions. In Figs. 2c and 2d, we see that the precipitation percentile corresponding to  $P_M$  for each grid point is different, and it ranges from 78.2nd to 90.6th for the seven monsoon divisions, indicating that a uniform extreme percentile (e.g., the 95th) may represent varying degrees of “extreme” for different monsoon regions. Note that the corresponding percentiles of  $P_M$  are usually lower than those of  $P_L$ , but both exhibit a consistent spatial pattern (Fig. S8).

#### b. Changes of the cutoff scale over the GM region

Previous studies have shown that the changes in the shape of the extreme tail can be well represented by rescaling the cutoff scale in observations and climate models (Neelin et al. 2017; Martinez-Villalobos and Neelin 2018; Chang et al. 2020). Moreover, a recent study (Martinez-Villalobos and Neelin 2021) has shown that the CMIP6 ensemble simulates well the extreme tail and  $P_L$  spatial pattern (although with a bias in magnitude), boosting confidence in the use of CMIP6 to evaluate future fractional changes in precipitation extremes. Compared to the historical period, percent changes

in  $P_M$ , calculated by averaging percent changes across all available models, for the three periods (near-term, midterm, and long-term) under four scenarios (SSP1–2.6, SSP2–4.5, SSP3–7.0, and SSP5–8.5), are displayed in Fig. 3. Not surprisingly, the increasing trends of  $P_M$ , projected over most regions become larger from the near term to the long term and from the lowest-emission (SSP1–2.6) to the highest-emission (SSP5–8.5) scenario. A detailed comparison of the increasing magnitudes of  $P_M$  under the SSP2–4.5 and SSP5–8.5 scenarios is presented in Table 1. In the long-term projection, for instance, the overall increase ( $41.2\% \pm 19.8\%$ , mean  $\pm$  standard error) under the SSP5–8.5 scenario over the whole GM region is in sharp contrast with that of the SSP2–4.5 ( $17.4\% \pm 7.4\%$ ), implying a greatly reduced risk (57.8%) of extreme precipitation for a moderate-emission scenario. Such a strong increase in precipitation extremes greatly exceeds the enhancement (5.75%) of the mean precipitation under the SSP5–8.5 scenario (Chen et al. 2020). However, differences exist for individual monsoon regions. In the case of the long-term projection under the SSP5–8.5 scenario, the largest increases of the cutoff scale are found over NAF ( $59.3\% \pm 34.8\%$ ) and SAS ( $50.2\% \pm 33.0\%$ ), whereas NAM and SAM witness smaller increases,  $27.4\% \pm 21.4\%$  and  $33.1\% \pm 18.5\%$  respectively.

Figure 4 displays the response rates of  $P_M$ , normalized by the increase in global mean surface temperature, for the whole GM region and its subregions. As can be seen, changes in the response rates are modest over the whole GM region and most subregions as the period or scenario varies (Fig. 4). For example, over the whole GM region (Table 2), the scenario-averaged response rate is only 19% less comparing the near-term ( $7.3\% \pm 2.6\% \text{ K}^{-1}$ ) to the long-term projection ( $8.7\% \pm 2.9\% \text{ K}^{-1}$ ). A similarly subtle change is also seen in

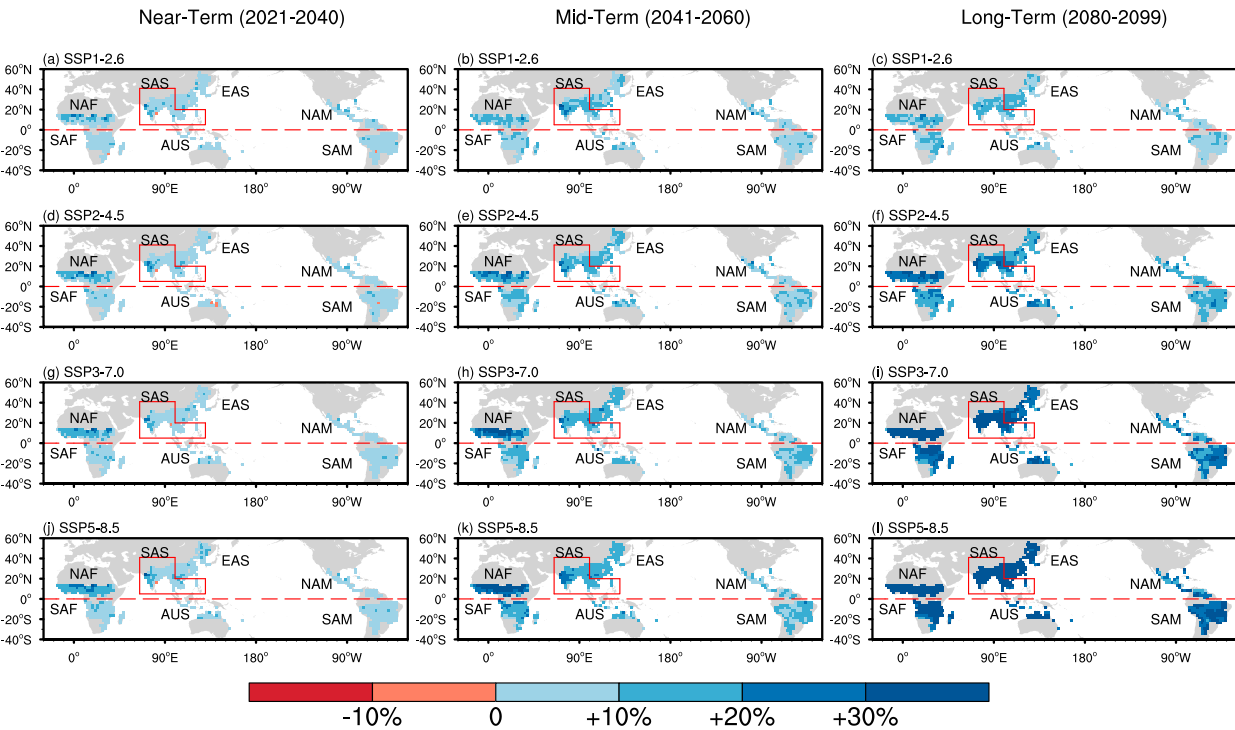


FIG. 3. Multimodel mean fractional changes of  $P_M$  over the GM region in the (left) near-term, (center) midterm, and (right) long-term projections under four scenarios relative to the historical period of 1995–2014.

the time-averaged rate from the low ( $7.3\% \pm 2.2\% \text{ K}^{-1}$ ) to the high ( $8.6\% \pm 2.8\% \text{ K}^{-1}$ ) emission scenario, and the statistically indistinguishable changes in response rates among different scenarios are also noted by Pendergrass et al. (2015). When taking the model spread into account, the projected response rate of  $P_M$  is nearly period-independent and scenario-independent over the whole GM region, and can be approximated to a constant  $8.0\% \text{ K}^{-1}$  by averaging all periods and scenarios, which is about 7.3 times higher than the sensitivity ( $1.1\% \text{ K}^{-1}$ ) of mean monsoon precipitation (Wang et al. 2020). Moreover, such features can also be found in most monsoon subregions. However, in the SAS and AUS regions, from the near term to the long term, the

scenario-averaged sensitivity has a robust fractional increase of 43% and 39%, respectively, while for the NAF region the time-averaged sensitivity is characterized with a strong fractional increase of 65% from the lowest to the highest emission scenario.

The projection of extreme monsoon precipitation may be affected by internal variability (Zhou et al. 2020). To understand the influence of the internal variability on the projection uncertainty, we make use of nine available models with at least three realizations (Table S2). By comparing the uncertainty (i.e., the standard deviation) in the increasing rates of single realization and multiple realizations, we found that the internal variability has little effect on

TABLE 1. Multimodel mean fractional changes of  $P_M$  over the whole GM region and its subregions in the near-term, midterm, and long-term projections under SSP2-4.5 and SSP5-8.5 scenarios. Values are shown as the mean  $\pm$  the standard error.

Region	SSP2-4.5			SSP5-8.5		
	Near-term	Midterm	Long-term	Near-term	Midterm	Long-term
GM	5.3% $\pm$ 2.5%	10.5% $\pm$ 4.5%	17.4% $\pm$ 7.4%	5.9% $\pm$ 2.4%	14.3% $\pm$ 5.7%	41.2% $\pm$ 19.8%
NAF	8.7% $\pm$ 5.4%	15.1% $\pm$ 8.3%	21.2% $\pm$ 10.4%	12.2% $\pm$ 7.4%	25.4% $\pm$ 13.5%	59.3% $\pm$ 34.8%
SAF	4.7% $\pm$ 3.0%	9.0% $\pm$ 5.0%	15.1% $\pm$ 7.0%	6.2% $\pm$ 3.9%	13.9% $\pm$ 7.5%	33.2% $\pm$ 15.0%
SAS	6.4% $\pm$ 5.6%	12.3% $\pm$ 7.4%	19.3% $\pm$ 10.8%	5.8% $\pm$ 3.9%	14.3% $\pm$ 8.3%	50.2% $\pm$ 33.0%
EAS	6.0% $\pm$ 2.9%	10.2% $\pm$ 4.5%	17.0% $\pm$ 8.0%	6.3% $\pm$ 3.4%	13.5% $\pm$ 6.2%	36.8% $\pm$ 16.3%
AUS	3.5% $\pm$ 5.4%	9.8% $\pm$ 8.6%	19.6% $\pm$ 13.3%	5.5% $\pm$ 7.8%	12.6% $\pm$ 9.3%	37.1% $\pm$ 29.1%
NAM	3.4% $\pm$ 3.8%	8.7% $\pm$ 6.9%	13.0% $\pm$ 8.8%	3.3% $\pm$ 3.7%	9.4% $\pm$ 5.6%	27.4% $\pm$ 21.4%
SAM	4.8% $\pm$ 3.7%	9.3% $\pm$ 5.3%	16.0% $\pm$ 9.7%	5.1% $\pm$ 3.5%	12.6% $\pm$ 7.0%	33.1% $\pm$ 18.5%



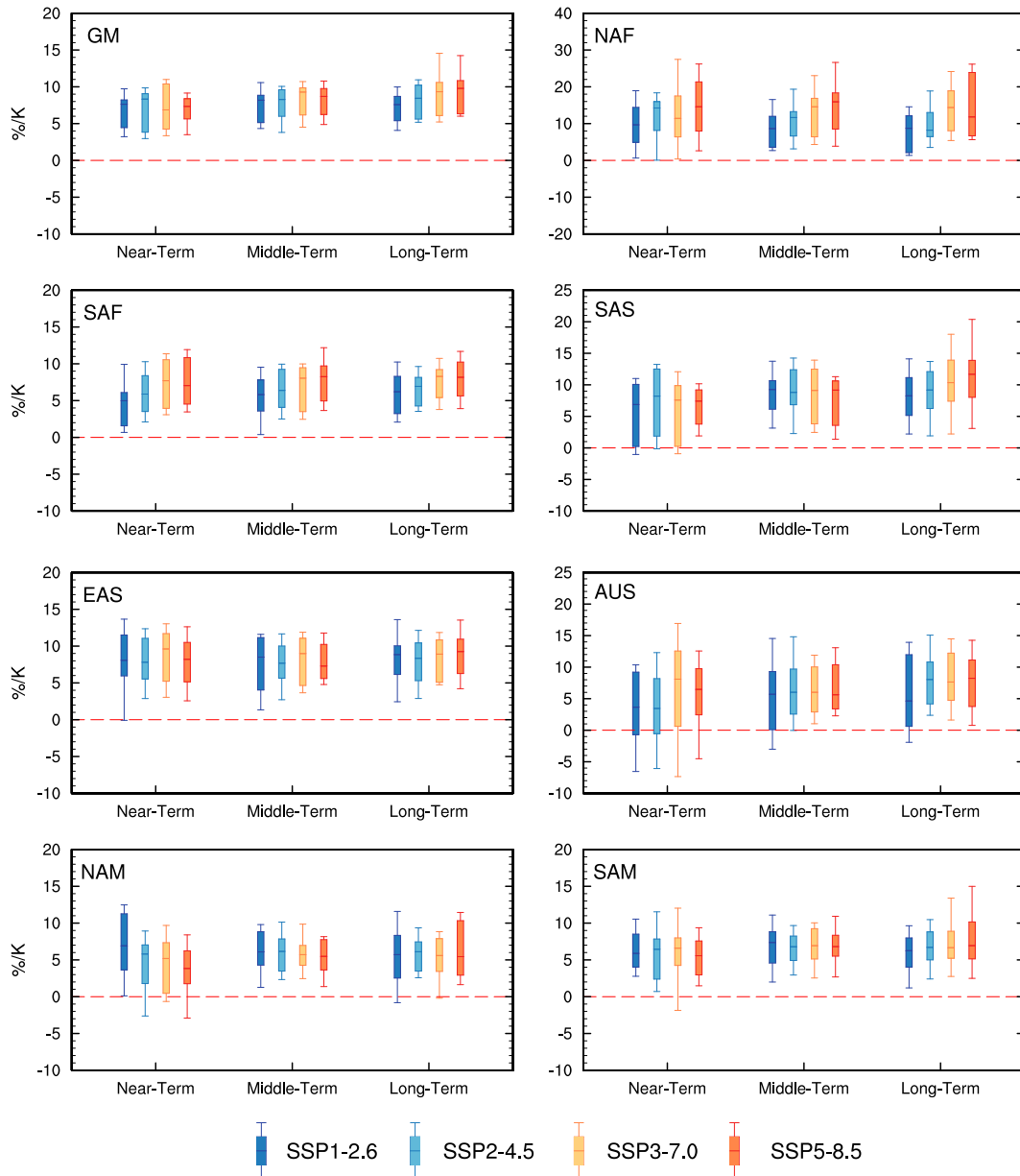


FIG. 4. The response rates of  $P_M$ , normalized by global mean surface temperature changes, over the whole GM region and seven monsoon subregions, in three periods and four scenarios. The bars denote the 10th–90th percentiles, and the boxes represent the 25th–75th percentiles in the CMIP6 models. The center lines in the boxes indicate the 50th percentile.

the uncertainty of projections in precipitation extremes (Table S3).

#### c. Changes of daily precipitation PDFs and risk of extreme precipitation

Changes in the cutoff scale can be regarded as the indicator of changes in the extreme tail of the daily precipitation probability distribution. With the extension of the cutoff scale, distinct upshifts of the extreme right tail of daily

precipitation PDFs are identified over the whole GM region in the long-term projection (Fig. 5). Moreover, the rescaled historical PDFs (the blue dotted line) with only rescaling historical  $P_L$  by the multimodel averaged increase of  $P_M$ , well matched the long-term projection PDFs (the blue solid line). For all four scenarios, the extreme tail demonstrates a consistent upward shift, implying a higher fraction of daily precipitation extremes over the GM region (Fig. 5a). This feature holds true for all seven individual

TABLE 2. The scenario-averaged and time-averaged response rates over the whole GM region and its subregions, derived from multimodel mean results. Values are shown as the mean  $\pm$  the standard error.

Region	Scenario-averaged response rate (% K <sup>-1</sup> )			Time-averaged response rate (% K <sup>-1</sup> )			
	Near-term	Midterm	Long-term	SSP1-2.6	SSP2-4.5	SSP3-7.0	SSP5-8.5
GM	7.3 $\pm$ 2.6	8.1 $\pm$ 2.4	8.7 $\pm$ 2.9	7.3 $\pm$ 2.2	7.7 $\pm$ 2.5	8.5 $\pm$ 2.9	8.6 $\pm$ 2.8
NAF	12.6 $\pm$ 7.8	12.6 $\pm$ 6.5	12.0 $\pm$ 6.6	9.2 $\pm$ 6.0	11.3 $\pm$ 5.8	13.9 $\pm$ 7.7	15.2 $\pm$ 8.3
SAF	6.7 $\pm$ 3.5	7.0 $\pm$ 3.2	7.4 $\pm$ 2.8	5.8 $\pm$ 3.2	6.7 $\pm$ 2.9	7.8 $\pm$ 3.4	7.9 $\pm$ 3.3
SAS	7.0 $\pm$ 5.1	8.7 $\pm$ 4.0	10.0 $\pm$ 5.2	7.8 $\pm$ 4.3	8.7 $\pm$ 4.8	8.8 $\pm$ 5.2	9.0 $\pm$ 4.8
EAS	8.5 $\pm$ 3.9	8.1 $\pm$ 3.2	8.6 $\pm$ 3.2	8.3 $\pm$ 3.9	8.2 $\pm$ 3.3	8.6 $\pm$ 3.3	8.4 $\pm$ 3.3
AUS	5.9 $\pm$ 8.3	6.9 $\pm$ 5.3	8.2 $\pm$ 5.8	5.5 $\pm$ 6.4	7.0 $\pm$ 6.0	7.6 $\pm$ 6.3	7.7 $\pm$ 7.2
NAM	5.2 $\pm$ 4.4	6.1 $\pm$ 3.1	6.2 $\pm$ 4.3	6.4 $\pm$ 4.1	5.7 $\pm$ 3.7	5.7 $\pm$ 3.9	5.4 $\pm$ 3.8
SAM	6.7 $\pm$ 4.9	7.2 $\pm$ 3.5	7.4 $\pm$ 3.9	7.0 $\pm$ 4.1	6.9 $\pm$ 4.0	7.3 $\pm$ 4.4	7.2 $\pm$ 4.0

monsoon regions, although the magnitude of the increase differs (Fig. 5b). Consistent with the largest increase in the cutoff scale over NAF, the most salient extension in the extreme tail of daily precipitation PDF is also observed there.

Figure 6 shows the risk ratios over the whole GM region for the long-term projections under all scenarios. In accordance with theory (Martinez-Villalobos and Neelin 2019) and observed risk ratios (Martinez-Villalobos and Neelin 2018; Chang et al. 2020), a rapid increase is seen in the extreme precipitation above the cutoff scale, with a stronger magnitude under the highest SSP5-8.5 emission scenario (Fig. 6). For example, for extreme precipitation exceeding the historical 99.9th percentile of precipitation  $P_{99.9}$ , in the long-term

projection the risk would increase to 3.61 (median value) times that in the historical period under the SSP5-8.5 scenario. This increase is 70% larger compared to the one projected under the SSP2-4.5 scenario (2.12) (Fig. 6). Regionally, higher risks in the long-term projection under the SSP5-8.5 scenario are witnessed in the NAF (4.97), NAM (3.9), EAS (4.16), and SAM (4.94) regions (Fig. S9).

#### d. Dynamic and thermodynamic contributions to future increases of precipitation extremes

To reveal mechanisms explaining these increases in precipitation extremes, we use the scaling relationship [(4)] to decompose the extreme precipitation into dynamic and thermodynamic contributions. Here the thermodynamic contribution only means the

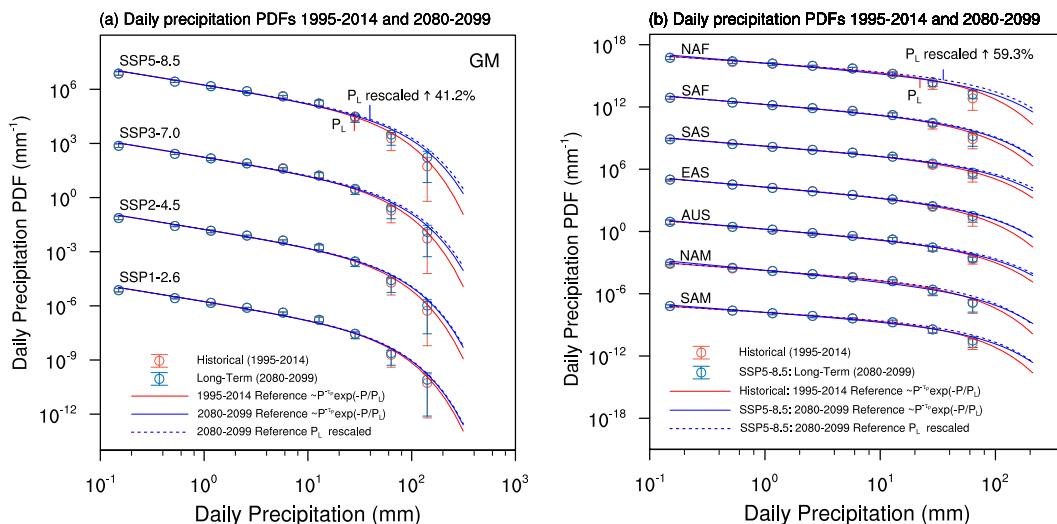


FIG. 5. (a) The PDFs of daily precipitation in the long term over the whole GM region under four scenarios (SSP1-2.6 PDFs  $\times 10^{-5}$ , SSP2-4.5 PDFs  $\times 10^{-1}$ , SSP3-7.0 PDFs  $\times 10^3$ , SSP5-8.5 PDFs  $\times 10^7$ ). (b) The PDFs of daily precipitation in the long term over the seven monsoon subregions under the SSP5-8.5 scenario (NAF PDFs  $\times 10^{17}$ , SAF PDFs  $\times 10^{13}$ , SAS PDFs  $\times 10^9$ , EAS PDFs  $\times 10^5$ , AUS PDFs  $\times 10^1$ , NAM PDFs  $\times 10^{-3}$ , SAM PDFs  $\times 10^{-7}$ ). For the solid lines and bars in (a) and (b), the red represents the historical period 1995–2014 and the blue represents the long term. The solid red lines and blue lines are fitted by (1), and the blue dotted lines are rescaled from historical period based on (1), with only rescaling  $P_L$  by the multimodel averaged changes of  $P_M$ . The bars represent the results from 21 CMIP6 models (10th–90th percentiles) and the circles indicate the median value.

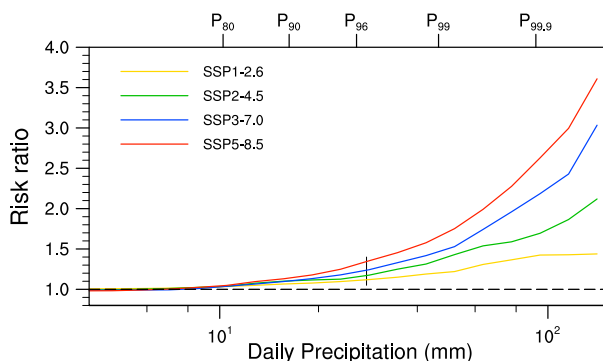


FIG. 6. The risk ratios (median value) calculated following (3) over the whole GM region in the long term under four scenarios. The black vertical line denotes the  $P_L$  of the multimodel mean in the historical period 1995–2014 and the coordinate of the top  $x$  axis is marked with different precipitation percentiles of the multimodel mean in the historical period 1995–2014.

effect of the specific humidity change. As shown in Fig. 7, the scaling relationship accurately reproduces the spatial distribution of mean extreme precipitation larger than  $P_M$  during the historical period 1995–2014 (Figs. 7a,b; spatial correlation of 0.97 and root-mean-square difference of  $2.7 \text{ mm day}^{-1}$ ). Moreover, the effectiveness of the scaling relationship in reproducing the changes in extreme precipitation is also accurately verified (Figs. 7c,d; spatial correlation of 0.88 and root-mean-square difference of 24%). Note that the precipitation extremes scaling also works well for other scenarios and periods with spatial correlations all greater than 0.8 (Table S4).

For the increases in precipitation extremes of the whole GM region, contributions from the thermodynamics are

comparable to those of dynamics (Fig. 8). The results of the multimodel mean show that the averaged thermodynamic and dynamic contributions across all three periods and all four scenarios account for about 51.5% and 48.5% in the changes of full scaling, respectively (Table S5). However, the relative importance of thermodynamic and dynamic contributions varies with regions. Regionally, changes in thermodynamic scaling dominate the increase in the SAF, EAS, NAM, and SAM regions, while changes in dynamic scaling are of more importance in the SAS, NAF, and AUS regions (Fig. 8), which is also verified by Table S5. In addition, over the GM region we show that the large intermodel scatter of the changes in precipitation extremes is highly consistent with that of the changes in the full scaling (Fig. 9). This distinct intermodel difference in the full-scaling changes exhibits a much stronger correlation with those of the changes in dynamic than thermodynamic scaling among models (Fig. 9; see also Fig. S10). Thus, the large intermodel spread of the projection in precipitation extremes is dominated by the uncertainty of dynamic contribution among models.

Compared to the homogeneous increase in thermodynamic scaling, changes in dynamic scaling exhibit pronounced regional contrast (Fig. 10). Overall, for the GM region, positive contributions from thermodynamics and dynamics are seen in most regions. However, the uneven spatial distribution in extreme precipitation changes mainly comes from the dynamic contribution (Fig. S11), which is also shown by previous studies (Pfahl et al. 2017; Wang et al. 2020). These spatial changes in thermodynamic and dynamic scaling correspond well to the changes in averaged vertically integrated saturation specific humidity  $q_s$  and vertical velocity  $\omega_e$  ( $\omega_e < 0$ ) of all days when extreme precipitation occurs, respectively (Fig. S12). Zonally, the

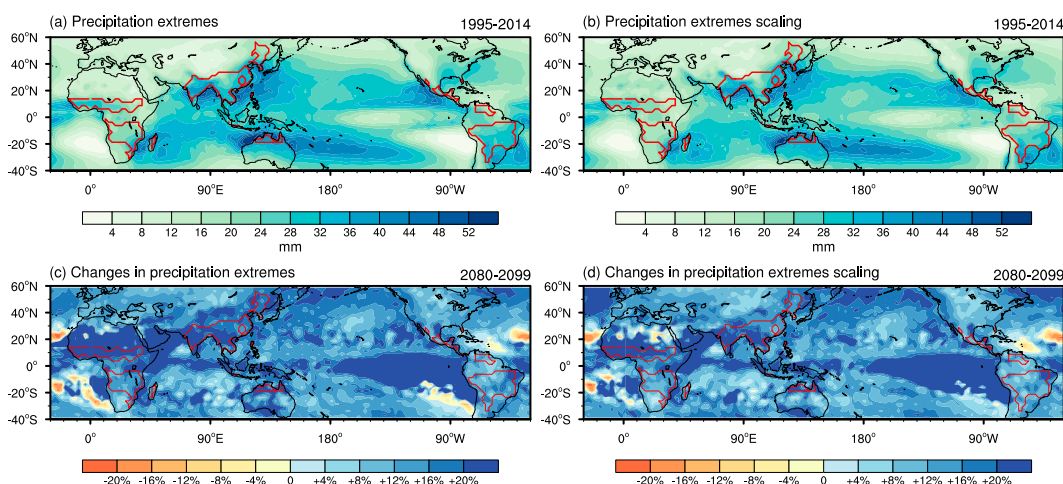


FIG. 7. Multimodel mean (a) precipitation extremes and (b) full scaling of extreme precipitation derived using (4) for all days with daily precipitation exceeding  $P_M$  in 1995–2014. Multimodel mean of fractional changes relative to the period 1995–2014 of (c) precipitation extremes and (d) full scaling for all days with daily precipitation exceeding  $P_M$  in the long term under SSP2–4.5 scenario. The red lines denote the boundaries of the global land monsoon region.



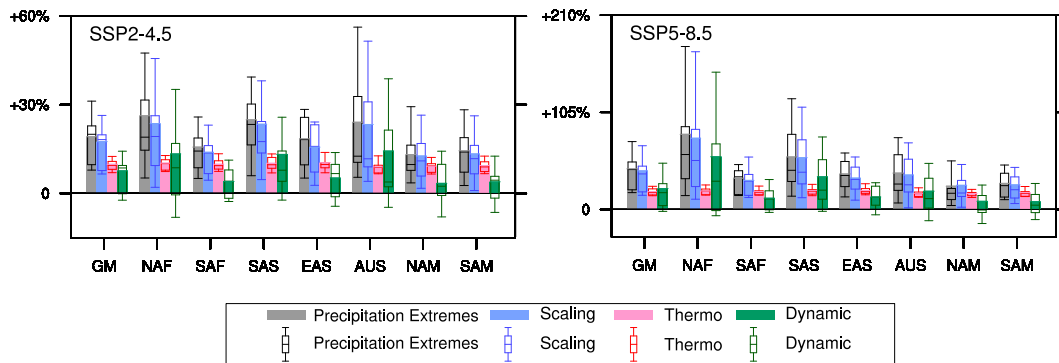


FIG. 8. Fractional changes relative to the period 1995–2014 in precipitation extremes, full scaling, thermodynamic scaling, and dynamic scaling for all days with daily precipitation exceeding  $P_M$  over the whole GM region and its subregions in the long-term under SSP2-4.5 and SSP5-8.5 scenarios. The bars denote the 10th–90th percentiles, and the boxes represent the spread of the 15 CMIP6 models (from the 25th to the 75th percentiles; the center lines indicate the 50th percentile). The histograms with colors indicate the multimodel ensemble mean.

increasing magnitude in thermodynamic scaling is nearly invariant with latitudes. In contrast, the magnitude of dynamic contribution shows a larger meridional fluctuation (Fig. 10), which dominates the regional difference of changes in precipitation extremes for the monsoon regions of different latitudes. Moreover, the zonal-mean dynamic contribution over the GM region is dominated by the dynamic changes of the SAS, NAF, and AUS monsoon regions (Fig. S8).

#### 4. Conclusions and discussion

In this study, we have examined changes in the daily precipitation cutoff scale to investigate global warming increases in precipitation extremes over the global land monsoon (GM) region in the CMIP6 ensemble.

For the GM region, the increasing magnitude of the cutoff scale is projected to be enhanced from the near term to the long term and from the low- to high-emission scenario. The increase in cutoff scale is associated with an upward shift in the daily precipitation PDF extreme tail. To first order, this upward shift can be economically captured by a simple rescaling of the PDF.

While the frequency of precipitation extremes will increase under any scenario considered, efforts to mitigate future warming can still produce a sizable positive impact. For example, we see a fractional reduction of 57.8% ( $17.4\% \pm 7.4\%$  vs  $41.2\% \pm 19.8\%$ ) in the cutoff scale in the SSP2-4.5 scenario compared with the SSP5-8.5 scenario in the long-term projection. This reduction can have a substantial effect on the frequency of the most extreme events, with days above 100 mm (approximately 99.9th percentile in historical period) in the GM region being about 1.7 times (median) more frequent in the SSP5-8.5 scenario than in the SSP2-4.5 scenario by the end of the century. Such features are also observed in seven individual monsoon subregions, in some cases with larger

increases (NAF, NAM, EAS, and SAM), but the magnitude differs.

The response rates of the cutoff scale, normalized by increases in global mean surface temperature, are nearly time-invariant and scenario-invariant over the GM region, which is roughly  $8.0\% \text{ K}^{-1}$ . From the near-term to the long-term projection, a narrow range of  $7.3\%–8.7\% \text{ K}^{-1}$  is found for the scenario-averaged rates, and meanwhile a similar subtle fluctuation of  $7.3\%–8.6\% \text{ K}^{-1}$  occurs in the time-averaged response rates from the SSP1-2.6 to SSP5-8.5 scenario. Similar near invariance in the periods or scenarios is also found in most monsoon subregions with the exceptions of NAF (the response rates vary with scenarios), SAS, and AUS (the response rates vary with periods) monsoon regions. This finding has important implications for determining the GM and regional monsoon response to anthropogenic forcing. Moreover, we show that the uncertainty in response rates is almost independent of internal variability, which may be masked by the large intermodel spread in projections. In addition, the effect of internal variability is also suppressed since changes are calculated based on the value of a 20-yr period.

Changes in the cutoff scale were separated in thermodynamic and dynamic contributions. For the GM region, the results from multimodel mean show that these contributions are comparable in the intensification of extreme precipitation. This is different from the enhancement of mean monsoon precipitation, which is apparently dominated by the contribution from thermodynamics (Chen et al. 2020). Regionally, the thermodynamic contribution dominates over the SAF, EAS, NAM, and SAM, while the dynamic contribution dominates over SAS, NAF, and AUS. Moreover, the thermodynamic scaling contributes to a uniform increase in extreme precipitation for all monsoon regions, while the dynamic scaling is responsible for the

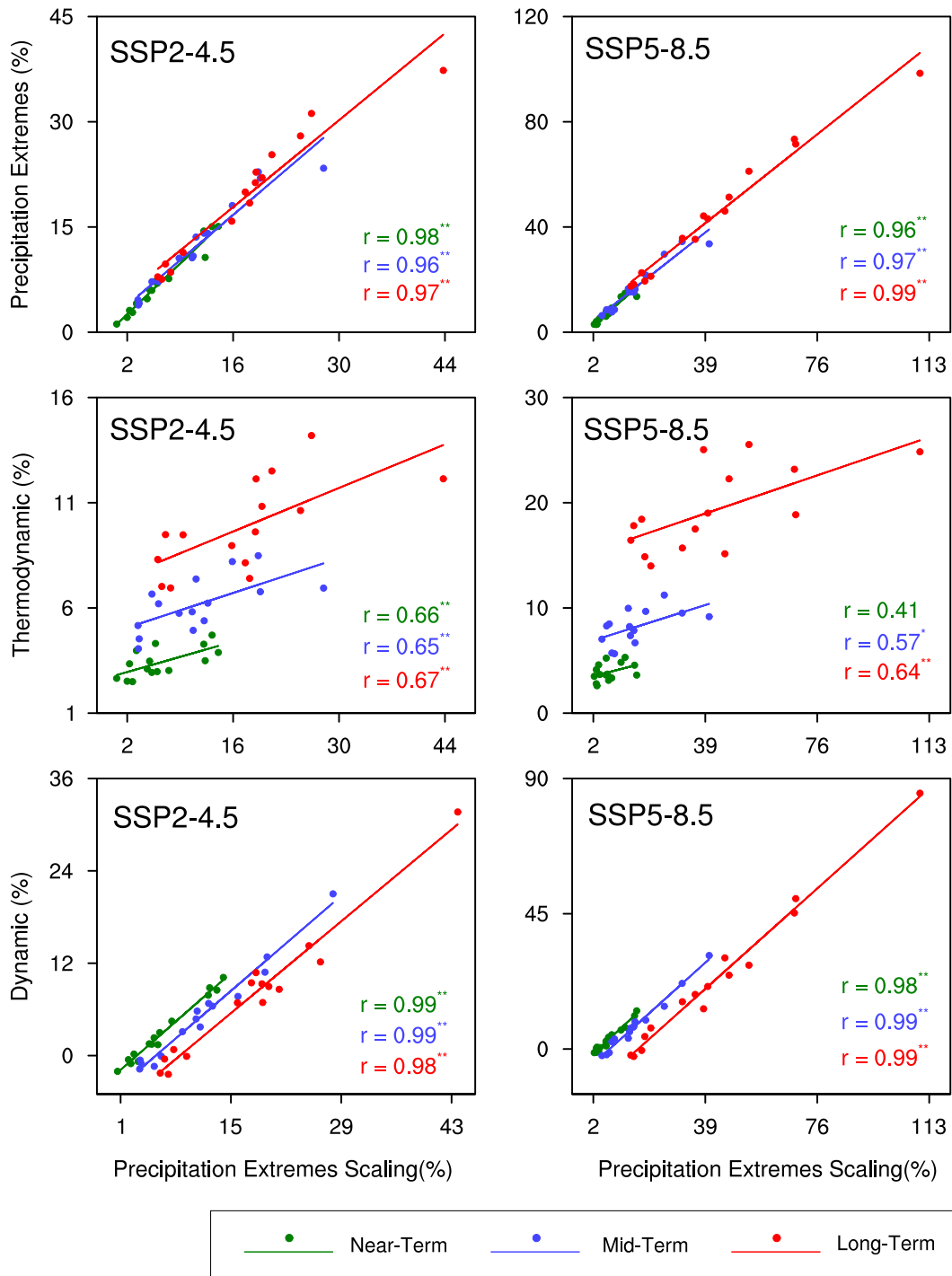


FIG. 9. Fractional changes in precipitation extremes scaling for each model vs changes in (top) precipitation extremes, (middle) thermodynamic scaling, and (bottom) dynamic scaling over the whole GM region under the SSP2-4.5 and SSP5-8.5 scenarios. The solid lines represent the linear fit, with correlation coefficient ( $r$ ). The asterisk represents a 5% of significance level and double asterisk represents a 1% of significance level.

regional variations. Also, the large intermodel scatter in the changes of precipitation extremes is also mainly contributed by the dynamic scaling. Overall, in response to climate warming, positive thermodynamics and dynamics

combined contribute to an increasing rate of  $\sim 8.0\% \text{ K}^{-1}$  in precipitation extremes for GM domain, implying an increasing risk beyond what we would expect simply by an increase in water vapor under any scenario.

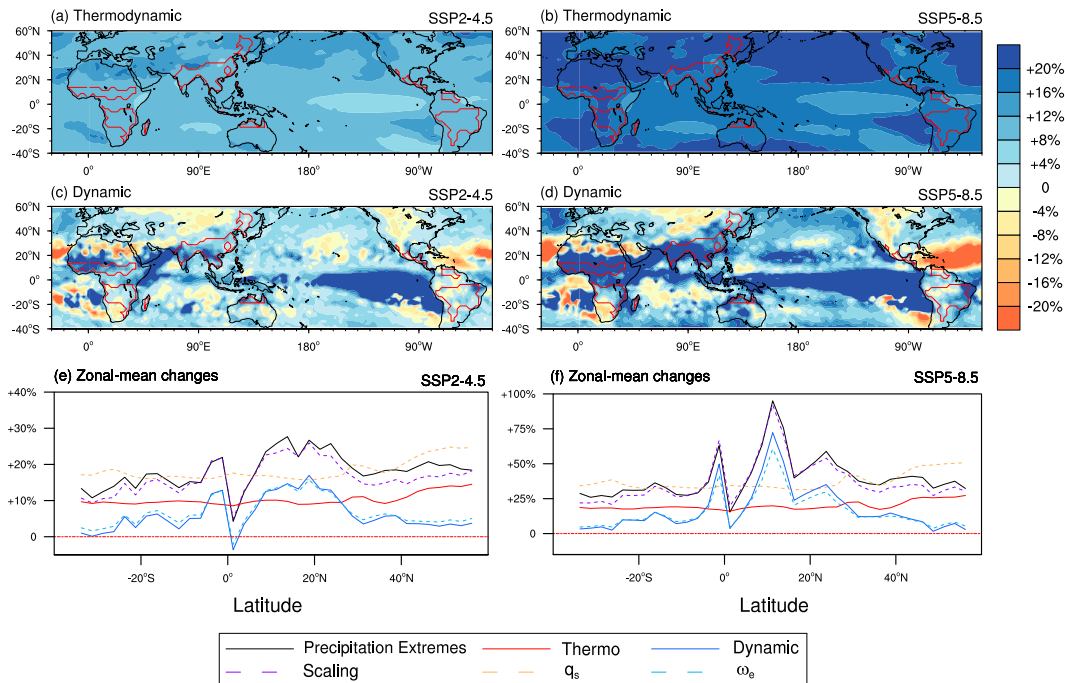


FIG. 10. Multimodel mean fractional changes in (a),(b) thermodynamic scaling and (c),(d) dynamic scaling for all days with daily precipitation exceeding  $P_M$  in the long term under SSP2-4.5 and SSP5-8.5 scenarios relative to the period 1995–2014. The red lines in (a)–(d) denote the boundaries of global land monsoon region. (e),(f) Zonally averaged changes relative to the period 1995–2014 in precipitation extremes, full scaling, thermodynamic scaling, dynamic scaling, vertically integrated saturation specific humidity  $q_s$ , and vertical velocity  $\omega_e$  for all days with daily precipitation exceeding  $P_M$  over the GM region in the long term under SSP2-4.5 and SSP5-8.5 scenarios. The lines in (e) and (f) represent the mean value of the 15 CMIP6 models.

**Acknowledgments.** This work was supported by the National Key R&D Program of China (2018YFA0605604) and by Proyecto Corfo Ingeniería 2030 código 14ENI2-26865 (CM-V).

## REFERENCES

- Adler, R. F., and Coauthors, 2003: The version-2 Global Precipitation Climatology Project (GPCP) monthly precipitation analysis (1979–present). *J. Hydrometeor.*, **4**, 1147–1167, [https://doi.org/10.1175/1525-7541\(2003\)004<1147:TVGPCP>2.0.CO;2](https://doi.org/10.1175/1525-7541(2003)004<1147:TVGPCP>2.0.CO;2).
- Alexander, L. V., and Coauthors, 2019: On the use of indices to study extreme precipitation on sub-daily and daily timescales. *Environ. Res. Lett.*, **14**, 125008, <https://doi.org/10.1088/1748-9326/ab51b6>.
- Ali, H., and V. Mishra, 2018: Contribution of dynamic and thermodynamic scaling on sub-daily precipitation extremes in India. *Geophys. Res. Lett.*, **45**, 2352–2361, <https://doi.org/10.1002/2018GL077065>.
- Allen, M. R., and W. J. Ingram, 2002: Constraints on future changes in the climate and the hydrological cycle. *Nature*, **419**, 228–232, <https://doi.org/10.1038/nature01092>.
- Chang, M., B. Liu, C. Martinez-Villalobos, G. Ren, S. Li, and T. Zhou, 2020: Changes in extreme precipitation accumulations during the warm season over continental China. *J. Climate*, **33**, 10 799–10 811, <https://doi.org/10.1175/JCLI-D-20-0616.1>.
- Chen, Z., T. Zhou, L. Zhang, X. Chen, W. Zhang, and J. Jiang, 2020: Global land monsoon precipitation changes in CMIP6 projections. *Geophys. Res. Lett.*, **47**, e2019GL086902, <https://doi.org/10.1029/2019GL086902>.
- Chevuturi, A., N. P. Klingaman, A. G. Turner, and S. Hannah, 2018: Projected changes in the Asian-Australian monsoon region in 1.5°C and 2.0°C global-warming scenarios. *Earth's Future*, **6**, 339–358, <https://doi.org/10.1002/2017EF000734>.
- Cho, H., K. P. Bowman, and G. R. North, 2004: A comparison of gamma and lognormal distributions for characterizing satellite rain rates from the tropical rainfall measuring mission. *J. Appl. Meteor.*, **43**, 1586–1597, <https://doi.org/10.1175/JAM2165.1>.
- Contractor, S., M. G. Donat, and L. V. Alexander, 2018: Intensification of the daily wet day rainfall distribution across Australia. *Geophys. Res. Lett.*, **45**, 8568–8576, <https://doi.org/10.1029/2018GL078875>.
- Deluca, A., and Á. Corral, 2010: Power laws and scaling of rain events and dry spells in the Catalonia region. 22 pp., <http://hdl.handle.net/2072/152168>.
- , and —, 2014: Scale invariant events and dry spells for medium-resolution local rain data. *Nonlinear Processes Geophys.*, **21**, 555–567, <https://doi.org/10.5194/npg-21-555-2014>.
- Deng, K., S. Yang, M. Ting, Y. Tan, and S. He, 2018: Global monsoon precipitation: Trends, leading modes, and associated drought and heat wave in the Northern Hemisphere. *J. Climate*, **31**, 6947–6966, <https://doi.org/10.1175/JCLI-D-17-0569.1>.

- Eyring, V., S. Bony, G. A. Meehl, C. A. Senior, B. Stevens, R. J. Stouffer, and K. E. Taylor, 2016: Overview of the Coupled Model Intercomparison Project phase 6 (CMIP6) experimental design and organization. *Geosci. Model Dev.*, **9**, 1937–1958, <https://doi.org/10.5194/gmd-9-1937-2016>.
- Freychet, N., H.-H. Hsu, C. Chou, and C.-H. Wu, 2015: Asian summer monsoon in CMIP5 projections: A link between the change in extreme precipitation and monsoon dynamics. *J. Climate*, **28**, 1477–1493, <https://doi.org/10.1175/JCLI-D-14-00449.1>.
- Giorgi, F., F. Raffaele, and E. Coppola, 2019: The response of precipitation characteristics to global warming from climate projections. *Earth Syst. Dyn.*, **10**, 73–89, <https://doi.org/10.5194/esd-10-73-2019>.
- Ha, K.-J., S. Moon, A. Timmermann, and D. Kim, 2020: Future changes of summer monsoon characteristics and evaporative demand over Asia in CMIP6 simulations. *Geophys. Res. Lett.*, **47**, e2020GL087492, <https://doi.org/10.1029/2020GL087492>.
- IPCC, 2014: Summary for policymakers. *Climate Change 2014: Impacts, Adaptation, and Vulnerability*, C. B. Field et al., Eds., Cambridge University Press, 1–32.
- Kirsch, T. D., C. Wadhvani, L. Sauer, S. Doocy, and C. Catlett, 2012: Impact of the 2010 Pakistan floods on rural and urban populations at six months. *PLOS Curr.*, **1**, 2432, <https://doi.org/10.1371/4dfdb212d2432>.
- Kitoh, A., H. Endo, K. Krishna Kumar, I. F. A. Cavalcanti, P. Goswami, and T. Zhou, 2013: Monsoons in a changing world: A regional perspective in a global context. *J. Geophys. Res. Atmos.*, **118**, 3053–3065, <https://doi.org/10.1002/jgrd.50258>.
- Lee, D., S.-K. Min, E. Fischer, H. Shiogama, I. Bethke, L. Lierhammer, and J. F. Scinocca, 2018: Impacts of half a degree additional warming on the Asian summer monsoon rainfall characteristics. *Environ. Res. Lett.*, **13**, 044033, <https://doi.org/10.1088/1748-9326/aab55d>.
- Lui, Y. S., C.-Y. Tam, and N.-C. Lau, 2019: Future changes in Asian summer monsoon precipitation extremes as inferred from 20-km AGCM simulations. *Climate Dyn.*, **52**, 1443–1459, <https://doi.org/10.1007/s00382-018-4206-3>.
- Martinez-Villalobos, C., and J. D. Neelin, 2018: Shifts in precipitation accumulation extremes during the warm season over the United States. *Geophys. Res. Lett.*, **45**, 8586–8595, <https://doi.org/10.1029/2018GL078465>.
- , and —, 2019: Why do precipitation intensities tend to follow gamma distributions? *J. Atmos. Sci.*, **76**, 3611–3631, <https://doi.org/10.1175/JAS-D-18-0343.1>.
- , and —, 2021: Climate models capture key features of extreme precipitation probabilities across regions. *Environ. Res. Lett.*, **16**, 024017, <https://doi.org/10.1088/1748-9326/abd351>.
- Mishra, V., and H. L. Shah, 2018: Hydroclimatological perspective of the Kerala flood of 2018. *J. Geol. Soc. India*, **92**, 645–650, <https://doi.org/10.1007/s12594-018-1079-3>.
- Moon, S., and K.-J. Ha, 2020: Future changes in monsoon duration and precipitation using CMIP6. *npj Climate Atmos. Sci.*, **3**, 45, <https://doi.org/10.1038/s41612-020-00151-w>.
- Neelin, J. D., S. Sahany, S. N. Stechmann, and D. Bernstein, 2017: Global warming precipitation accumulation increases above the current-climate cutoff scale. *Proc. Natl. Acad. Sci. USA*, **114**, 1258–1263, <https://doi.org/10.1073/pnas.1615333114>.
- Ni, Y., and P.-C. Hsu, 2018: Inter-annual variability of global monsoon precipitation in present-day and future warming scenarios based on 33 Coupled Model Intercomparison Project Phase 5 models. *Int. J. Climatol.*, **38**, 4875–4890, <https://doi.org/10.1002/joc.5704>.
- O’Gorman, P. A., and T. Schneider, 2009a: Scaling of precipitation extremes over a wide range of climates simulated with an idealized GCM. *J. Climate*, **22**, 5676–5685, <https://doi.org/10.1175/2009JCLI2701.1>.
- , and —, 2009b: The physical basis for increases in precipitation extremes in simulations of 21st-century climate change. *Proc. Natl. Acad. Sci. USA*, **106**, 14 773–14 777, <https://doi.org/10.1073/pnas.0907610106>.
- O’Neill, B. C., and Coauthors, 2016: The Scenario Model Intercomparison Project (ScenarioMIP) for CMIP6. *Geosci. Model Dev.*, **9**, 3461–3482, <https://doi.org/10.5194/gmd-9-3461-2016>.
- Pall, P., M. R. Allen, and D. A. Stone, 2007: Testing the Clausius–Clapeyron constraint on changes in extreme precipitation under CO<sub>2</sub> warming. *Climate Dyn.*, **28**, 351–363, <https://doi.org/10.1007/s00382-006-0180-2>.
- Pendergrass, A. G., 2018: What precipitation is extreme? *Science*, **360**, 1072–1073, <https://doi.org/10.1126/science.aat1871>.
- , F. Lehner, B. M. Sanderson, and Y. Xu, 2015: Does extreme precipitation intensity depend on the emissions scenario? *Geophys. Res. Lett.*, **42**, 8767–8774, <https://doi.org/10.1002/2015GL065854>.
- Peters, O., C. Hertlein, and K. Christensen, 2001: A complexity view of rainfall. *Phys. Rev. Lett.*, **88**, 018701, <https://doi.org/10.1103/PhysRevLett.88.018701>.
- , A. Deluca, A. Corral, J. D. Neelin, and C. E. Holloway, 2010: Universality of rain event size distributions. *J. Stat. Mech.*, **2010**, P11030, <https://doi.org/10.1088/1742-5468/2010/11/P11030>.
- Pfahl, S., P. A. O’Gorman, and E. M. Fischer, 2017: Understanding the regional pattern of projected future changes in extreme precipitation. *Nat. Climate Change*, **7**, 423–427, <https://doi.org/10.1038/nclimate3287>.
- Seth, A., A. Giannini, M. Rojas, S. A. Rauscher, S. Bordoni, D. Singh, and S. J. Camargo, 2019: Monsoon responses to climate changes—Connecting past, present and future. *Curr. Climate Change Rep.*, **5**, 63–79, <https://doi.org/10.1007/s40641-019-00125-y>.
- Stechmann, S. N., and J. D. Neelin, 2011: A stochastic model for the transition to strong convection. *J. Atmos. Sci.*, **68**, 2955–2970, <https://doi.org/10.1175/JAS-D-11-028.1>.
- , and —, 2014: First-passage-time prototypes for precipitation statistics. *J. Atmos. Sci.*, **71**, 3269–3291, <https://doi.org/10.1175/JAS-D-13-0268.1>.
- Sugiyama, M., H. Shiogama, and S. Emori, 2010: Precipitation extreme changes exceeding moisture content increases in MIROC and IPCC climate models. *Proc. Natl. Acad. Sci. USA*, **107**, 571–575, <https://doi.org/10.1073/pnas.0903186107>.
- Trenberth, K. E., A. Dai, R. M. Rasmussen, and D. B. Parsons, 2003: The changing character of precipitation. *Bull. Amer. Meteor. Soc.*, **84**, 1205–1218, <https://doi.org/10.1175/BAMS-84-9-1205>.
- Vera, C., and Coauthors, 2006: Toward a unified view of the American monsoon systems. *J. Climate*, **19**, 4977–5000, <https://doi.org/10.1175/JCLI3896.1>.
- Wang, B., and Q. Ding, 2008: Global monsoon: Dominant mode of annual variations in the tropics. *Dyn. Atmos. Oceans*, **44**, 165–183, <https://doi.org/10.1016/j.jdynatmoce.2007.05.002>.
- , H.-J. Kim, K. Kikuchi, and A. Kitoh, 2011: Diagnostic metrics for evaluation of annual and diurnal cycles. *Climate Dyn.*, **37**, 941–955, <https://doi.org/10.1007/s00382-010-0877-0>.

- , C. Jin, and J. Liu, 2020: Understanding future change of global monsoons projected by CMIP6 models. *J. Climate*, **33**, 6471–6489, <https://doi.org/10.1175/JCLI-D-19-0993.1>.
- Wang, X., D. Jiang, and X. Lang, 2017: Future extreme climate changes linked to global warming intensity. *Sci. Bull.*, **62**, 1673–1680, <https://doi.org/10.1016/j.scib.2017.11.004>.
- Wu, J., B. Zhou, and Y. Xu, 2015: Response of precipitation and its extremes over China to warming: CMIP5 simulation and projection. *Chin. J. Geophys.*, **58**, 461–473, <https://doi.org/10.1002/cjg2.20187>.
- Zhang, D.-L., Y. Lin, P. Zhao, X. Yu, S. Wang, H. Kang, and Y. Ding, 2013: The Beijing extreme rainfall of 21 July 2012: “Right results” but for wrong reasons. *Geophys. Res. Lett.*, **40**, 1426–1431, <https://doi.org/10.1002/grl.50304>.
- Zhang, W., and T. Zhou, 2019: Significant increases in extreme precipitation and the associations with global warming over the global land monsoon regions. *J. Climate*, **32**, 8465–8488, <https://doi.org/10.1175/JCLI-D-18-0662.1>.
- , —, L. Zou, L. Zhang, and X. Chen, 2018: Reduced exposure to extreme precipitation from 0.5°C less warming in global land monsoon regions. *Nat. Commun.*, **9**, 3153, <https://doi.org/10.1038/s41467-018-05633-3>.
- Zhou, T., J. Lu, W. Zhang, and Z. Chen, 2020: The sources of uncertainty in the projection of global land monsoon precipitation. *Geophys. Res. Lett.*, **47**, e2020GL088415, <https://doi.org/10.1029/2020GL088415>.